



Coupling overall water splitting and biomass oxidation via Fe-doped Ni₂P@C nanosheets at large current density

Di Li^a, Zengyong Li^a, Ren Zou^a, Ge Shi^{a,b}, Yiming Huang^a, Wu Yang^a, Wang Yang^a, Chuanfu Liu^{a,*}, Xinwen Peng^{a,*}

^a State Key Laboratory of Pulp and Paper Engineering, School of Light Industry and Engineering, South China University of Technology, 381 Wushan Road, Guangzhou 510641, PR China

^b Centre for Catalysis and Clean Energy, Griffith University, Southport, QLD 4222, Australia

ARTICLE INFO

Keywords:

Bifunctional electrocatalysts
Overall water splitting
Biomass monosaccharide oxidation
DFT calculation

ABSTRACT

Developing efficient bifunctional electrocatalyst for overall water splitting and conversion of biomass into value-added products at large current density is essential but challenging. Herein, a hierarchical Fe-doped Ni₂P nanosheets hybridized with C on Ni foam (Fe-Ni₂P@C/NF) was developed as a robust bifunctional catalyst with excellent catalytic activity for hydrogen evolution reaction (HER) with overpotentials of 75 and 313 mV at 10 and 1000 mA cm⁻², respectively, and as well as for OER with a lower overpotential of 269 mV at 400 mA cm⁻². Particularly, the integrated double-electrode electrolyzer for simultaneous HER and biomass-derived monosaccharide oxidation reaction (MOR) using Fe-Ni₂P@C/NF only requires a low voltage of 1.55 V to drive a current density of 100 mA cm⁻². Meanwhile, the value-added lactic acid is obtained at the anode. This strategy of coupling biomass oxidation to promote H₂ production can significantly reduce energy consumption and obtain additional high value-added products.

1. Introduction

Electrocatalytic water splitting for the production of clean and sustainable H₂ has been considered as a cost-effective and promising technology to alleviate the increasingly depleting fossil energy [1,2]. In general, water electrolysis involves two core half-reactions, including cathodic hydrogen evolution reaction (HER) and anodic oxygen evolution reaction (OER), which requires highly efficient electrocatalyst to accelerate the reaction kinetics and consequently reduce the overpotentials [3]. Precious Pt-based and Ir/Ru-based materials have been identified as advanced electrocatalysts for HER and OER, respectively. However, their widespread applications are limited owing to the high cost and scarcity of these precious metals [4,5]. At present, several transition metal-based electrocatalysts, such as transition-metal phosphides [6–8], nitrides [9,10], carbides [11,12], selenides [13,14] and sulfides [15] with high activity for HER and OER have been developed to replace noble metal-based catalysts. However, it has been recently reported that bifunctional catalysts generally exhibit high activity for a single reaction, and most of them perform well only at lower current densities, thereby resulting in the requirement for higher overpotential

at large current densities (300–500 mA cm⁻²) [16]. Therefore, the development of efficient bifunctional electrocatalysts, particularly with excellent catalytic activity for both HER and OER at large current densities, is of great significance for industrial-scale electrolysis of water for H₂ production, but it is also challenging.

In addition, during the overall water splitting process, the O₂ produced at the anode is relatively insignificant and also inevitably mixed with H₂ produced at the cathode, which consequently increases the risk factor [17]. Therefore, it is particularly important to substitute the sluggish OER by utilizing more thermodynamically favorable oxidation reaction [18]. Recently, several organic substrate molecules such as hydrazine [19–21], alcohols [22,23], urea [24–26], and amines [27] are used as sacrificial agents for electrochemical oxidation to replace the anodic OER. Moreover, 5-hydroxymethylfurfural oxidation has also been used to promote HER and produce value-added chemicals [28,29]. This chemical-reagent-assisted strategy has played a significant role in reducing the voltage of water electrolysis and promoting H₂ production. However, most of the above chemicals are either expensive or toxic, and even the by-products such as N₂ and CO₂ are also generated at the anode, which limit the practical applications of H₂ production through

* Corresponding authors.

E-mail addresses: chfliu@scut.edu.cn (C. Liu), fexwpeng@scut.edu.cn (X. Peng).

<https://doi.org/10.1016/j.apcatb.2022.121170>

Received 15 November 2021; Received in revised form 13 January 2022; Accepted 31 January 2022

Available online 2 February 2022

0926-3373/© 2022 Published by Elsevier B.V.

water splitting.

To solve the above problems, electrochemical oxidation of renewable biomass or biomass-derived intermediates to produce high value-added products as an alternative anode reaction is a promising strategy. Monosaccharide is a class of small-molecule sugars, derived from lignocellulosic biomass, such as glucose, arabinose, xylose, and fructose, that can be oxidized into various value-added chemicals (organic acid) [30]. Lactic acid, one of the oxidation products of the above mentioned sugars, is a valuable platform chemical widely used in the fields of food, medicine, chemical industry, and articles for daily use [31,32]. It is interesting to note that the polylactic acid (PLA) prepared from lactic acid, as a biodegradable plastic, can replace fossil-derived plastics, which is beneficial in preventing environmental pollution [33]. At present, fermentation and chemical catalysis are the main methods for preparing lactic acid. In actual production, the development of lactic acid through fermentation is restricted owing to the complicated separation and purification processes, high equipment cost, and high energy consumption [34]. In recent years, the production of lactic acid through chemical catalysis using biomass resources has been widely developed. For example, Onda et al. [35] reported the oxidation of glucose by Pt/C catalyst to obtain lactic acid with a yield of 45% at 80 °C. Lin et al. [36] investigated xylose oxidation over ZrO₂ catalyst to obtain lactic acid with a yield of 40% at 200–220 °C. Moreover, LaCoO₃ catalyst converted xylose to lactic acid with N₂ (2.8 MPa) with a yield of 38% at 200 °C [37]. Although synthesizing lactic acid through conventional chemical catalysis can provide a certain yield, harsh conditions such as high temperature and pressure, and the use of precious metal catalyst will cause additional energy consumption and increase in cost. Therefore, owing to high energy efficiency and operation at normal temperature and pressure, electrochemical oxidation is a more sustainable alternative for the oxidation of monosaccharide to produce lactic acid. Hence, replacing anodic OER by monosaccharide oxidation reaction (MOR) would be a promising strategy, which can reduce energy consumption and produce H₂ at cathode and more valuable lactic acid at anode simultaneously. In addition, recent advances demonstrate that the transition metal phosphides (TMPs) can be act as bifunctional electrocatalyst for both HER and biomass oxidation due to their superior electrical conductivity, mechanical strength and chemical stability [38, 39]. However, high overpotential is still required at large current density by utilizing TMPs based catalysts for HER or biomass oxidation. Doping metal atoms into the lattices of metal phosphides can further adjust the atomic coordination and electronic structure, optimize the adsorption and desorption energy of the reactants, and thus improve the catalytic activity [40]. Thus, developing the efficient TMPs based bifunctional electrocatalyst to integrate HER and biomass oxidation at large current density is highly attractive and desirable.

In this work, a hierarchical Fe-doped Ni₂P nanosheets hybridized with C on Ni foam (Fe-Ni₂P@C/NF) was fabricated as a robust bifunctional electrocatalyst for both HER and MOR. The Fe-atom doping could modulate the electronic structure of Ni₂P, thus optimizing the adsorption and dissociation energy of H₂O (ΔG_{H_2O}) and reducing H adsorption free energy (ΔG_{H^*}). Moreover, the enhanced electrical conductivity of the catalyst owing to the carbon layer can further facilitate the electron transfer, thereby enhancing the HER and OER performances. Interestingly, the Fe-Ni₂P@C/NF catalyst exhibits superior catalytic performance for both the HER and OER at large current density with low overpotentials and small Tafel slopes. Meanwhile, Fe-Ni₂P@C/NF also exhibits excellent catalytic activity for coupling the HER and MOR, in which arabinose is employed for the MOR and only a cell voltage as low as 1.55 V is required to achieve the current density of 100 mA cm⁻². In addition, the yield of lactic acid obtained at the anode is 52.1%, and other biomass-derived monosaccharides such as xylose, glucose, and fructose are also selected for the MOR to replace the OER and coupling with HER to boost H₂ production.

2. Experimental section

2.1. Chemicals

Nickel (II) nitrate hexahydrate (Ni(NO₃)₂·6H₂O) and potassium hydroxide (KOH) were purchased from Aladdin Reagents Ltd. Iron (III) nitrate nonahydrate (Fe(NO₃)₃·9H₂O) was purchased from Tianjin Damao Chemical Reagent Ltd. Urea, ammonium fluoride (NH₄F), glucose and xylose were purchased from Aladdin Reagents Ltd. Arabinose, fructose and sodium hypophosphite (NaH₂PO₂) were purchased from Macklin. Nickel foam (NF) was purchased from Kunshan Guangjiayuan Electronics Co Ltd.

2.2. Synthesis of NiFe(OH)_x/NF

Nickel foam (NF) was first cleaned in 3 M HCl for 2 h and then washed several times with deionized water and ethanol. NiFe(OH)_x/NF was synthesized by using a facile hydrothermal method. In detail, 1.24 mmol of Fe(NO₃)₃·9H₂O, 1.72 mmol of Ni(NO₃)₂·6H₂O, 11.65 mmol of urea, and 5.41 mmol of NH₄F were dissolved in 80 mL of deionized water with continuous stirring to form a homogeneous solution. The mixture was then poured into a 100 mL Teflon autoclave. A piece of NF was immersed into the mixture, and the autoclave was subsequently sealed and maintained at 180 °C for 12 h. Thereafter, NF was again washed several times with deionized water and ethanol, and then dried at 60 °C for 12 h to obtain the NiFe(OH)_x/NF.

2.3. Synthesis of Fe-Ni₂P@C/NF, Fe-Ni₂P/NF and Ni₂P@C/NF

The as-synthesized NiFe(OH)_x/NF was transferred to 20 mL of a glucose solution (0.12 M) and kept for 10 h. It was then dried at 60 °C to obtain the NiFe(OH)_x@G/NF precursor. Thereafter, 0.5 g of NaH₂PO₂ and NiFe(OH)_x@G/NF were placed on the upstream and center of a quartz tube, respectively, and heated at 320 °C for 2 h with a heating rate of 2 °C min⁻¹ in an Ar atmosphere, yielding final Fe-Ni₂P@C/NF with a catalyst loading of approximately 2.4 mg cm⁻². Fe-Ni₂P/NF and Ni₂P@C/NF were also synthesized for comparison. The synthesis process of Fe-Ni₂P/NF and Ni₂P@C/NF was similar to the Fe-Ni₂P@C/NF, except that Fe-Ni₂P/NF was not treated with glucose and Ni₂P@C/NF was not doped with Fe atoms.

2.4. Characterization

The phase of catalyst was characterized by X-ray diffraction measurement (XRD) patterns with the Germany Bruker diffractometer. The X-ray photoelectron spectroscopy (XPS) was carried out to obtain the chemical composition of catalysts (Thermo Scientific NEXSA). The morphology of samples was observed by using SEM (Zeiss, Germany) and TEM (JEM-2100 F). Raman spectra were recorded on a Raman microscope (HJY LabRAM Aramis).

2.5. Electrode preparation and electrochemical measurement

All electrochemical measurements were carried out at the electrochemical workstation, and detailed electrode preparation and electrochemical tests are described in the [Supporting information](#).

3. Results and discussion

3.1. Synthesis, morphology and structure characterization

The scheme of the synthetic route of Fe-Ni₂P@C/NF is illustrated in Fig. 1a. The NiFe(OH)_x nanosheets were first grown on Ni foam (NF) through a hydrothermal reaction. Scanning electron microscopy (SEM) images of NiFe(OH)_x/NF show the hierarchical structure assembled from various nanosheets (Fig. S1). The crystalline phase of NiFe(OH)_x/

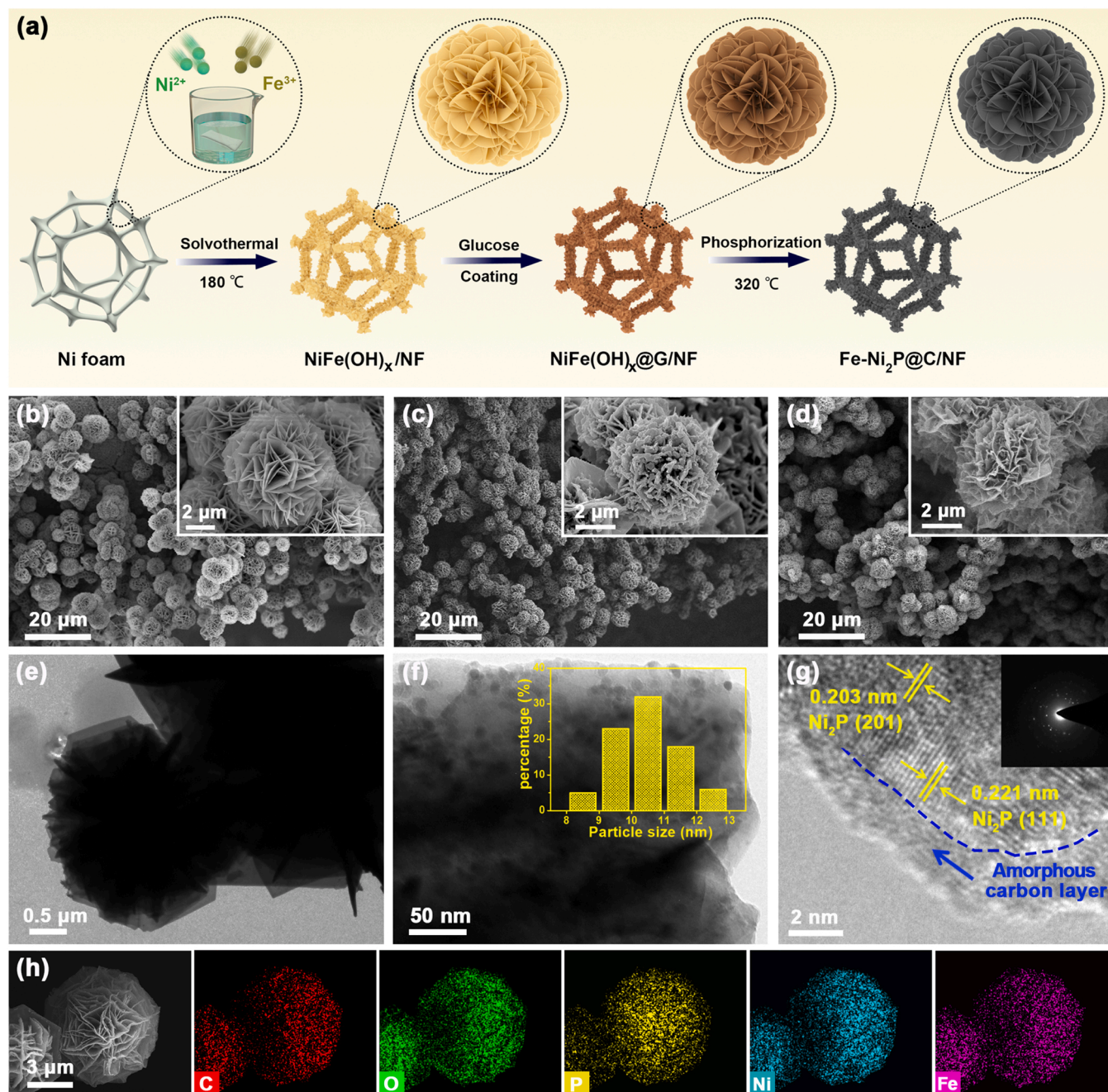


Fig. 1. (a) Illustration of the synthesis process of Fe-Ni₂P@C/NF. (b-d) SEM images of Fe-Ni₂P@C/NF, Fe-Ni₂P/NF and Ni₂P@C/NF, respectively. (e-g) TEM and HRTEM images of Fe-Ni₂P@C/NF, and (h) elemental mapping images of Fe-Ni₂P@C/NF. The inset in (g) is the SAED pattern.

NF was characterized through X-ray diffraction (XRD), which was well matched with NiFe-layered double hydroxides (NiFe-LDH) (PDF#51-0463) (Fig. S2). Thereafter, the as-prepared NiFe(OH)_x/NF was soaked in a glucose solution for 10 h, followed by a pyrolysis and phosphorization process under Ar gas flow, yielding the hierarchical nanosheets structure of Fe-Ni₂P@C/NF. As shown in Fig. 1b, the morphology of Fe-Ni₂P@C/NF is similar to that of NiFe(OH)_x/NF, which maintains the hierarchical nanosheets structure during the phosphorization process. Such hierarchical three-dimensional structure composed of nanosheets can also expose a larger surface area, which is beneficial to provide more active sites for catalytic reactions. The Brunauer–Emmett–Teller (BET) surface area of Fe-Ni₂P@C/NF (29.3 m² g⁻¹) is higher than that of Fe-Ni₂P/NF (14.8 m² g⁻¹), indicating that the carbon layer can further improve the BET surface area of the catalyst (Fig. S3). On the contrary,

the nanosheets structure of Fe-Ni₂P/NF without coating of carbon layer was destroyed after phosphorization (Fig. 1c), indicating that the carbon layer formed by the precursor plays a supporting role to well-maintain the nanosheets structure when treated with glucose. Meanwhile, the morphology of Ni₂P@C/NF without Fe doping was also investigated (Fig. 1d). Similar hierarchical structure can be observed, except for the wrinkled nanosheets. Moreover, transmission electron microscopy (TEM) images further confirm the hierarchical structure of

Fe-Ni₂P@C/NF (Fig. 1e). As shown in Fig. 1f, it can be clearly observed that the nanosheet is composed of nanoparticles with an average particle size of approximately 10.4 nm. The energy dispersive spectroscopy (EDS) was further carried out, which can confirm the presence of C, O, P, Ni and Fe elements (Fig. S4). In addition, the relative content of Ni and Fe elements are detected by ICP with the value of

92.59 and 1.86 wt%, respectively. The high-resolution TEM (HRTEM) image shown in Fig. 1g shows few amorphous carbon layers attached to Fe-Ni₂P with a thickness of approximately 2 nm. For comparison, Fe-Ni₂P/NF without glucose treatment was also investigated (Fig. S5), and no amorphous carbon layer was observed around Fe-Ni₂P. Raman spectroscopy was performed to further analyze the structures of Fe-Ni₂P@C/NF and Fe-Ni₂P/NF (Fig. S6). Indeed, Fe-Ni₂P@C/NF exhibits two typical characteristic peaks at 1350 and 1590 cm⁻¹, which are related to the disordered sp³ carbon (D band) and graphitic sp² carbon (G band), respectively. However, no peaks can be observed in the Fe-Ni₂P/NF sample, which further confirms the formation of the carbon layer in Fe-Ni₂P@C/NF. This is consistent with the results obtained from TEM measurements. The lattice fringe spacing of 0.221 nm and 0.203 nm are assigned to the (111) and (201) crystal planes of Ni₂P, respectively, and the selected area electron diffraction (SAED) pattern (inset in Fig. 1g) can further verify the polycrystalline structure of Fe-Ni₂P. Furthermore, the elemental mapping (Fig. 1h) demonstrates uniform distribution of C, O, P, Ni and Fe elements in Fe-Ni₂P@C/NF, thereby confirming the successful synthesis of Fe-Ni₂P@C/NF.

The crystal structures of Fe-Ni₂P@C/NF, Fe-Ni₂P/NF and Ni₂P@C/NF were investigated using the XRD spectra. As shown in Fig. 2a and Fig. S7, except for the peaks of Ni foam (PDF#04-0850), all the diffraction peaks of Fe-Ni₂P@C/NF and Fe-Ni₂P/NF correspond well with the Ni₂P phase (PDF#03-0953) with no diffraction peaks of Fe-related crystal phases, thus indicating that the incorporation of Fe atoms

did not change the crystal phase of Ni₂P during the phosphorization process. Furthermore, the detailed surface chemical composition and elemental state of the as-prepared catalysts were analyzed through X-ray photoelectron spectroscopy (XPS). As shown in Fig. 2b, the C, O, P, Ni and Fe elements were clearly observed in the survey spectra, thus confirming the successful incorporation of Fe atoms. The high-resolution C 1s spectrum (Fig. 2c) can be fitted into three peaks located at 284.5, 285.8 and 286.7 eV, which correspond to C=C/C-C, C-O/C-P and C=O, respectively [41]. For the P 2p spectrum shown in Fig. 2d, the peaks located at 129.4, 130.6 and 133.8 eV can be assigned to P 2p_{3/2}, P 2p_{1/2} and P-O, respectively [6]. The high-resolution Ni 2p spectra shows that the two main peaks located at 874.8 and 856.9 eV are associated with Ni

2p_{1/2} and Ni 2p_{3/2}, respectively (Fig. 2e) [42]. The peaks located at 853.7 and 870.8 eV can be ascribed to the Ni-P species in Ni₂P, while the peaks at 862.7 and 880.5 eV correspond to the satellite peaks [43]. As shown in Fig. 2f, the Fe 2p spectrum of Fe-Ni₂P@C/NF can be deconvoluted into two main peaks located at 712.8 and 725.1 eV, which correspond to Fe 2p_{3/2} and Fe 2p_{1/2}, respectively, and the peak at 710.7 and 724.1 eV can be attributed to the Fe²⁺ species [44]. Notably, no characteristic peaks of Fe-P were detected, further confirming the successful synthesis of Fe-Ni₂P@C/NF, which is consistent with the XRD characterization. In addition, compared to the bare Ni₂P@C/NF, the binding energies of P 2p and Ni 2p in the Fe-Ni₂P@C/NF catalyst exhibit a slight negative shift after Fe doping, thereby suggesting that the introduction of the Fe atoms could modulate the electronic structure of Ni₂P.

3.2. Electrocatalytic performance of HER

The electrocatalytic HER activity of Fe-Ni₂P@C/NF and compared samples were first evaluated using a three-electrode system under 1 M KOH medium, and a commercial Pt/C catalyst loaded on NF was also measured for reference. As shown in Fig. 3a, the relevant linear sweep voltammetry (LSV) curves show that Fe-Ni₂P@C/NF has the highest catalytic performance toward HER compared to other samples. The corresponding overpotentials at different current densities for the catalysts are shown in Fig. 3b. The Fe-Ni₂P@C/NF catalyst exhibits a lower overpotential of 75 mV to obtain a current density of 10 mA cm⁻² compared to Fe-Ni₂P/NF (125 mV) and Ni₂P@C/NF (209 mV), thereby indicating that Fe atom doping can enhance the catalytic performance toward the HER. Moreover, compared to the Fe-Ni₂P/NF catalyst, the Fe-Ni₂P@C/NF catalyst exhibits significantly enhanced HER performance, thus revealing the synergy between Fe-Ni₂P and the carbon layer. Notably, the overpotentials of Fe-Ni₂P@C/NF required for achieving large current density of 500 and 1000 mA cm⁻² are only 294 and 313 mV, respectively. The required overpotentials are lower than those in the cases of Fe-Ni₂P/NF (389 and 468 mV), Ni₂P@C/NF (462 and 514 mV), and even the commercial Pt/C catalyst (338 and 474 mV), which demonstrates the excellent catalytic performance of Fe-Ni₂P@C/

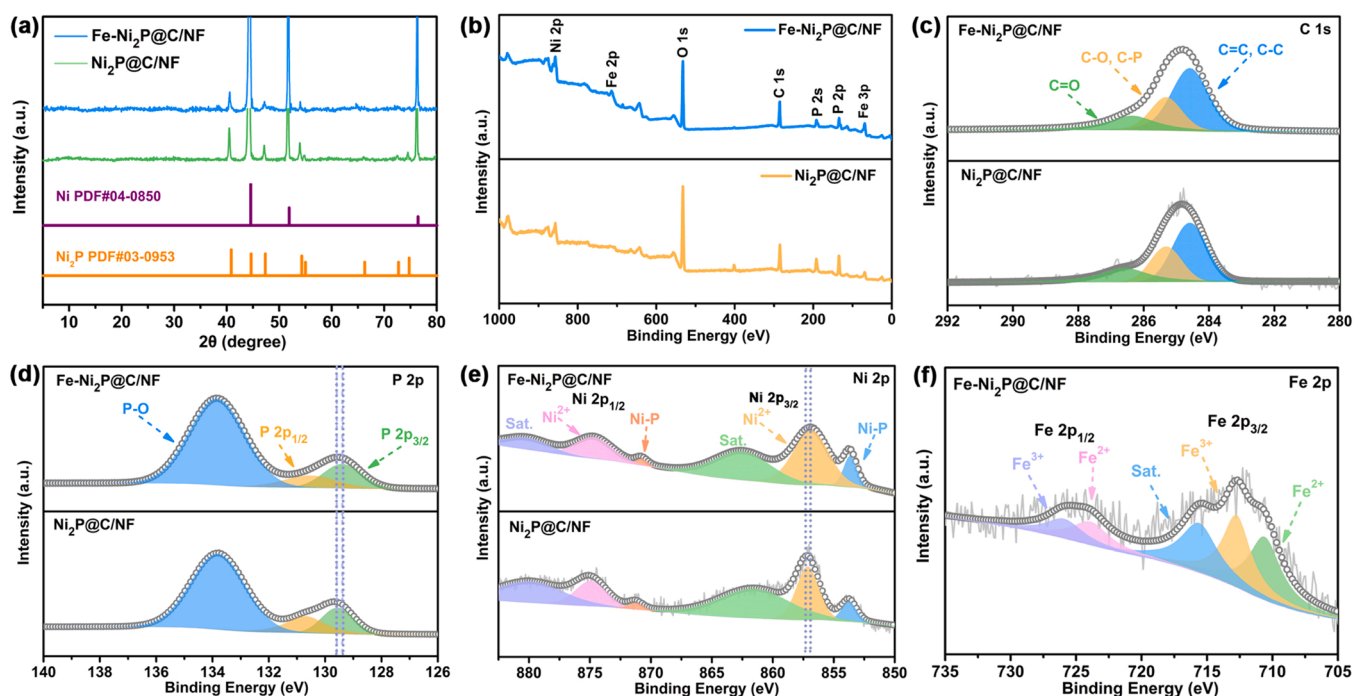


Fig. 2. (a) XRD spectra of the catalyst samples. (b) The XPS survey of Fe-Ni₂P@C/NF and Ni₂P@C/NF. The high-resolution spectra of (c) C 1s, (d) P 2p and (e) Ni 2p for Fe-Ni₂P@C/NF and Ni₂P@C/NF, and (f) Fe 2p for Fe-Ni₂P@C/NF.

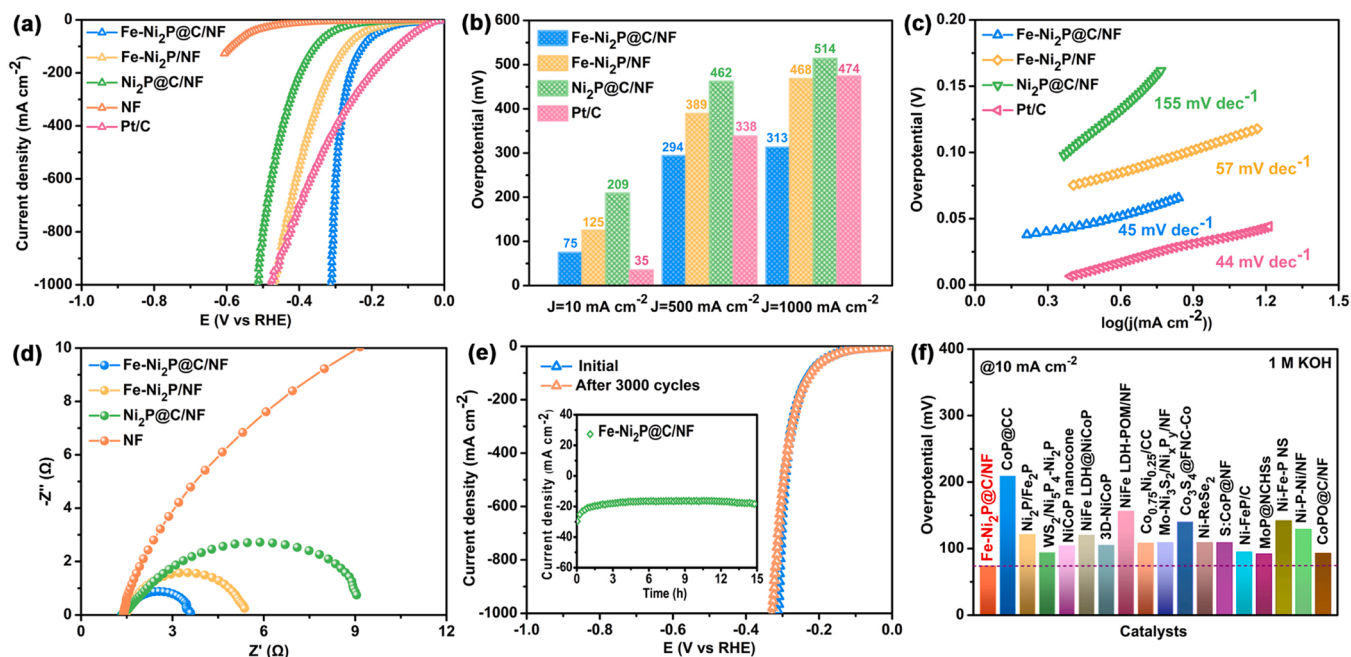


Fig. 3. (a) HER polarization curves and (b) corresponding overpotentials at different current densities of Fe-Ni₂P/C/NF, Fe-Ni₂P/NF, Ni₂P/C/NF, NF, and Pt/C for HER in 1 M KOH. (c) The corresponding Tafel slopes of electrocatalysts. (d) Nyquist plots of Fe-Ni₂P/C/NF and compared samples for HER in 1 M KOH. (e) 3000 CV cycles of Fe-Ni₂P/C/NF in 1 M KOH solution and the inset in (e) is the chronoamperometric curves. (f) Comparison of the overpotential at the current density of 10 mA cm⁻² for the Fe-Ni₂P/C/NF with other TM-based catalysts.

NF toward HER at large current density. The corresponding Tafel slope of Fe-Ni₂P/C/NF is 45 mV dec⁻¹, which is significantly smaller than those of Fe-Ni₂P/NF (57 mV dec⁻¹) and Ni₂P/C/NF (155 mV dec⁻¹), and similar to the commercial Pt/C catalyst (44 mV dec⁻¹) (Fig. 3c), which suggests more rapid catalytic kinetics toward HER. To further understand the intrinsic catalytic activity of Fe-Ni₂P/C/NF, electrochemical active surface area (ECSA) and electrochemical impedance spectroscopy (EIS) measurements were conducted. The ECSA of the as-prepared catalysts were estimated from the double-layer capacitance (C_{dl}), which is obtained from the CV curves versus different scanning rates (Fig. S8). As shown in Fig. S8d, the C_{dl} of Fe-Ni₂P/C/NF (98.4 mF cm⁻²) is significantly higher than those of Fe-Ni₂P/NF (55.2 mF cm⁻²) and Ni₂P/C/NF (41.9 mF cm⁻²), thereby implying that there are more exposed active sites in the Fe-Ni₂P/C/NF catalyst. The Nyquist plots (Fig. 3d) show that among all the samples, the Fe-Ni₂P/C/NF catalyst exhibits lowest charge-transfer resistance (R_{ct}) of 2.32 Ω, revealing the faster electron transfer rate. It can be attributed to the carbon layer that can provide continuous electron transfer channels, enhance the electrical conductivity, and further improve the catalytic performance of the electrocatalyst [45–47]. Furthermore, the stability of the Fe-Ni₂P/C/NF catalyst was evaluated from the CV cycles and long-term chronoamperometry in 1 M KOH. The polarization curves of Fe-Ni₂P/C/NF, depicted in Fig. 3e, display no obvious attenuation after 3000 cycles. Furthermore, the stable current–time curves (inset in Fig. 3e and Fig. S9) demonstrate that Fe-Ni₂P/C/NF catalyst exhibits no significant change of electrochemical performance even during 24 h reaction, further highlighting the excellent durability of it at large current density. In particular, these results indicate that the Fe-Ni₂P/C/NF catalyst exhibits outstanding catalytic performance toward the HER, which is also superior to several other reported non-noble-metal-based catalysts (Fig. 3f and Table S1). To further elucidate the stability of the Fe-Ni₂P/C/NF catalyst after the HER, the morphology and chemical composition of the catalyst after continuous HER test for 24 h were characterized using SEM and XPS. The SEM images show that the Fe-Ni₂P/C/NF catalyst retained the initial nanosheets structure, indicating that the morphology of Fe-Ni₂P/C/NF remained unchanged after

the HER (Fig. S10). In addition, the high-resolution spectrums of Ni 2p and P 2p reveal that the chemical composition is basically unchanged as compared to those from the initial sample, which further demonstrates the excellent long-time stability of the Fe-Ni₂P/C/NF catalyst (Fig. S11).

3.3. Electrocatalytic performance of OER and overall water splitting

The OER catalytic performance of Fe-Ni₂P/C/NF was then evaluated in 1 M KOH solution. As shown in Fig. 4a, the Fe-Ni₂P/C/NF catalyst also exhibits the highest catalytic activity for OER at high current density compared to other samples. Moreover, the catalyst is even superior to commercial IrO₂, revealing its enhanced OER performance after Fe doping. The corresponding overpotentials of the catalysts at different current densities shown in Fig. 4b show that the Fe-Ni₂P/C/NF catalyst only requires 255 and 269 mV to achieve the current densities of 200 and 400 mA cm⁻², respectively. These overpotential values are much lower than that of Fe-Ni₂P/NF (307 and 360 mV), Ni₂P/C/NF (470 and 602 mV) and IrO₂ (437 and 522 mV). As shown in Fig. 4c, the Fe-Ni₂P/C/NF catalyst has the smallest Tafel slope of 64 mV dec⁻¹ among all the as-prepared catalysts, indicating the faster kinetics of

Fe-Ni₂P/C/NF for OER. Similarly, the Fe-Ni₂P/C/NF exhibits the largest ECSA (Fig. S12). The smallest R_{ct} value (Fig. S13) further demonstrates the outstanding charge transport kinetics during the OER process. It is noteworthy that the electrocatalytic activity of Fe-Ni₂P/C/NF toward OER is also superior to those of the most recently reported catalysts (Table S2). In addition, the excellent durability of the Fe-Ni₂P/C/NF catalyst was confirmed by the LSV test after 3000 CV scans (Fig. S14). Negligible decay of the current density was observed after continuous long-time operation for over 24 h (Fig. S15). Furthermore, the morphology analysis from SEM images of Fe-Ni₂P/C/NF suggests that the catalyst retains its nanosheets structure even after the OER test, which confirms the excellent durability of the catalyst (Fig. S16). Indeed, the surface of the nanosheets becomes significantly rough and is covered by a thin layer of particles, which might be the oxide species formed due to the in-situ oxidation of the catalyst surface during the

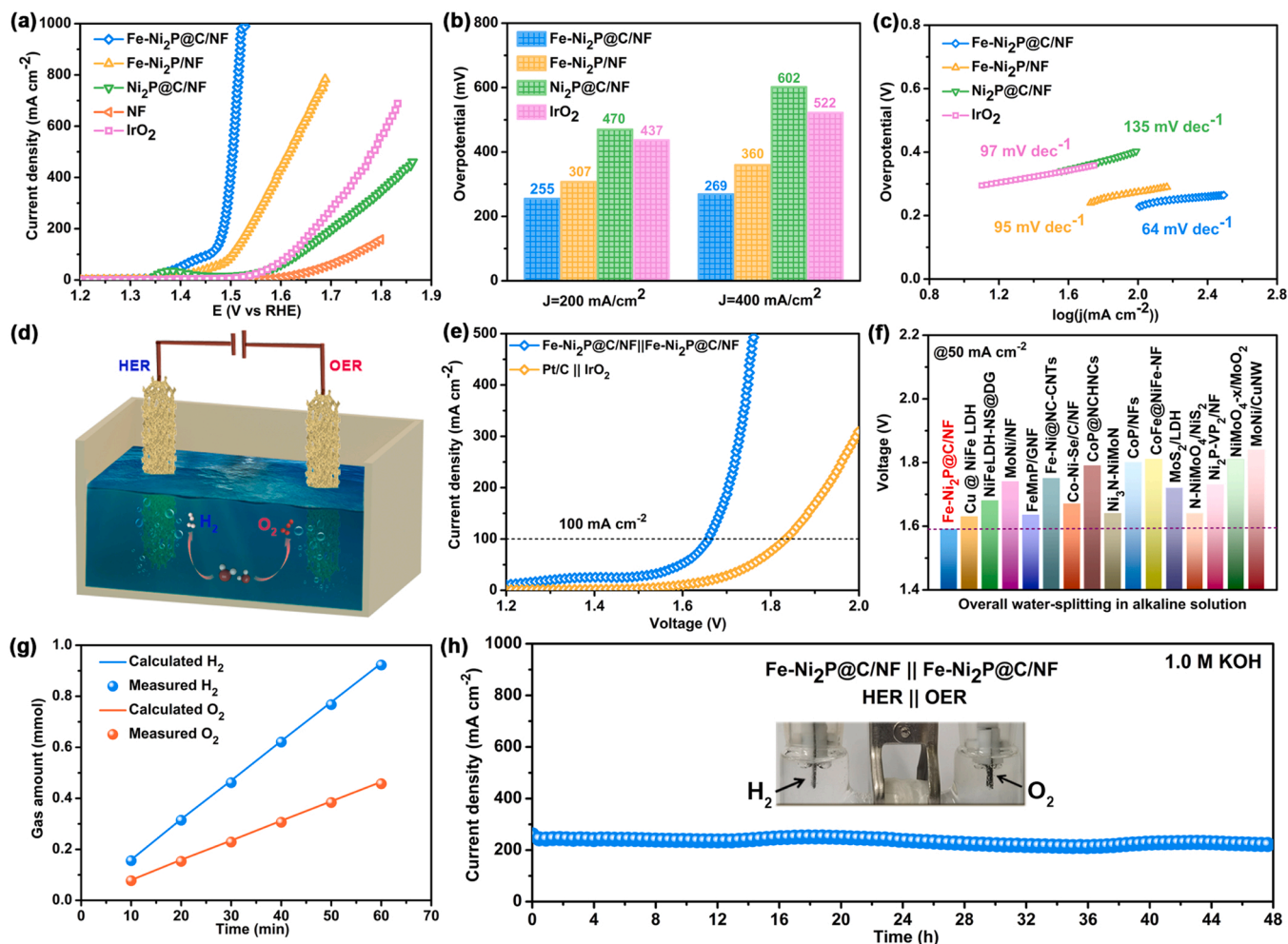


Fig. 4. (a) OER polarization curves and (b) corresponding overpotentials of electrocatalyst at 200 and 400 mA cm⁻² in 1 M KOH. (c) The corresponding Tafel slopes of samples for OER. (d) Schematic illustration of an electrolyzer for overall water splitting. (e) The polarization curves of Fe-Ni₂P/C/NF || Fe-Ni₂P/C/NF and Pt/C (-) || IrO₂ (+) electrode in 1 M KOH at 5 mV s⁻¹ in a two-electrode system for overall water splitting. (f) Comparison of the cell voltages at the current density of 50 mA cm⁻² of Fe-Ni₂P/C/NF with recently reported TM-based bifunctional electrocatalysts for overall water splitting. (g) Measured and theoretical gaseous products by the two-electrode system in 1 M KOH. (h) The Chronopotentiometric curves of water electrolysis at 1.7 V for 48 h in 1 M KOH.

OER process. To understand the chemical composition of the catalyst surface, the XPS measurement was conducted (Fig. S17). The characteristic peaks for Ni-P at 853.7 and 870.8 eV are not observed in the high-resolution Ni 2p spectra after OER test, which reveals that the Fe-Ni₂P/C/NF surface has oxidized into nickel oxide species. In addition, the attenuation of P signal in the P 2p spectra and the appearance of the typical Ni-O peak at 529.8 eV in the O 1s spectrum further confirm the formation of Ni oxide species, which is in accordance to the previous studies [48,49]. The XRD pattern of Fe-Ni₂P/C/NF after OER test shows the attenuation and disappearance of diffraction peaks of Ni₂P-related crystalline phase (Fig. S18), revealing the oxidation of Fe-Ni₂P/C/NF during the OER process, which is consistent with XPS analysis results. Moreover, the typical characteristic peaks of nickel oxide in the Raman spectra of Fe-Ni₂P/C/NF after OER test (Fig. S19) further confirms the formation of nickel oxide species [25]. On the base of the above results and previous reports, the formation of Ni oxide can be attributed to the in-situ electrochemical oxidation of the catalyst surface, which serves as the actual active sites with high electrochemical activity and stability toward the OER [50,51]. Based on the above electrochemical results, Fe-Ni₂P/C/NF exhibits outstanding catalytic activity for both HER and OER. Consequently, a double-electrode electrolyzer of Fe-Ni₂P/C/NF || Fe-Ni₂P/C/NF was assembled, which serves as a robust bifunctional catalyst to assess the catalytic activity for overall water splitting in alkaline media (Fig. 4d). For a comparative study, the commercial

catalysts Pt/C || IrO₂ were also analyzed under the same condition. As shown in Fig. 4e, Fe-Ni₂P/C/NF || Fe-Ni₂P/C/NF electrode exhibits a high catalytic activity with a cell voltage of 1.59 V to achieve the current density of 50 mA cm⁻². Notably, only a small cell voltage of 1.66 V is required for Fe-Ni₂P/C/NF || Fe-Ni₂P/C/NF electrode to drive a current density of 100 mA cm⁻², and it is significantly lower than that of Pt/C || IrO₂ electrode (1.83 V), suggesting the excellent catalytic activity for overall water splitting. Particularly, such high catalytic performance of Fe-Ni₂P/C/NF || Fe-Ni₂P/C/NF electrode is also superior to the most recently reported transition-metal-based bifunctional catalysts for overall water splitting (Fig. 4f and Table S3). We also compared the experimentally obtained amounts of H₂ and O₂ generated during the overall water splitting process with the theoretically calculated amount of gas to estimate the Faradaic efficiency. As shown in Fig. 4g, the experimentally obtained molar ratio of H₂ to O₂ is close to the theoretical value (2:1), revealing a nearly 100% Faradaic efficiency for water splitting. Moreover, the long-time durability of the electrocatalyst for overall water splitting at large current density was further evaluated shown in Fig. 4h. Fe-Ni₂P/C/NF || Fe-Ni₂P/C/NF electrode exhibits a negligible change at large current density even after 48 h, thereby demonstrating the excellent durability of the catalyst for overall water splitting.

3.4. Electrocatalytic performance of MOR

To further investigate the catalytic performance of Fe-Ni₂P@C/NF toward MOR at anode, a series of electrochemical tests were also conducted in 1 M KOH solution containing different monosaccharides. As shown in Fig. 5a, the polarization curves of Fe-Ni₂P@C/NF for MOR and OER (without arabinose) in 1 M KOH are compared. In the absence of arabinose, Fe-Ni₂P@C/NF exhibits a certain OER activity, which achieves the current density of 100 mA cm⁻² at a potential of 1.458 V. After introducing 20 mM arabinose, the potential for the same current density is significantly decreased to 1.362 V. Fig. 5b displays the corresponding potentials at different current densities in the presence of arabinose, which are lower than that required for the OER, thereby suggesting more highly catalytic activity of Fe-Ni₂P@C/NF for arabinose oxidation than the OER. Moreover, Fe-Ni₂P@C/NF exhibits a smaller Tafel slope for the arabinose oxidation (54 mV dec⁻¹) compared to the OER (64 mV dec⁻¹) (Fig. 5c), which further confirms that the catalytic reaction kinetics for MOR is more favorable. Based on the above electrochemical results, we believe that Fe-Ni₂P@C/NF could synchronously act as a robust bifunctional electrocatalyst for both HER and MOR. A double-electrode electrolyzer which consists of Fe-Ni₂P@C/NF || Fe-Ni₂P@C/NF as cathode and anode was also constructed to respectively generate H₂ and lactic acid (Fig. 5d). For comparison, the pure overall water splitting

process was also analyzed in the absence of monosaccharides. As shown in Fig. 5e, after the addition of arabinose, the voltage of the electrolyzer is decreased due to the substitution of OER by the favorable monosaccharide oxidation. Indeed, Fe-Ni₂P@C/NF || Fe-Ni₂P@C/NF electrode exhibits the cell voltage as small as 1.55 V to achieve the current density of 100 mA cm⁻² upon the addition of 20 mM arabinose, which is lower than that of pure water splitting (1.66 V). This reveals the high catalytic activity of the catalyst toward HER coupling with arabinose oxidation compared to overall water splitting. Such a lower cell voltage is comparable and even better than several reported bifunctional electrocatalysts for the coupling of H₂ production and anodic organic molecules oxidation (Table S4). Similarly, the performance of Fe-Ni₂P@C/NF || Fe-Ni₂P@C/NF for the other monosaccharide (xylose, glucose and fructose) oxidation coupling with HER was also evaluated (Fig. 5f), revealing the advantage of this strategy. Moreover, the chronoamperometry tests were carried out on the dual-electrode electrolyzer with monosaccharide addition, which shows that the current decreases to the initial state due to the nearly complete conversion of monosaccharide after long-term electrolysis (Fig. S20). Meanwhile, the H₂ production can be observed at the cathode, while no bubbles were generated at the anode during the chronoamperometry test (Fig. S21), which confirms that the oxidation of the monosaccharide precedes the competing OER. In order to further evaluate the durability and

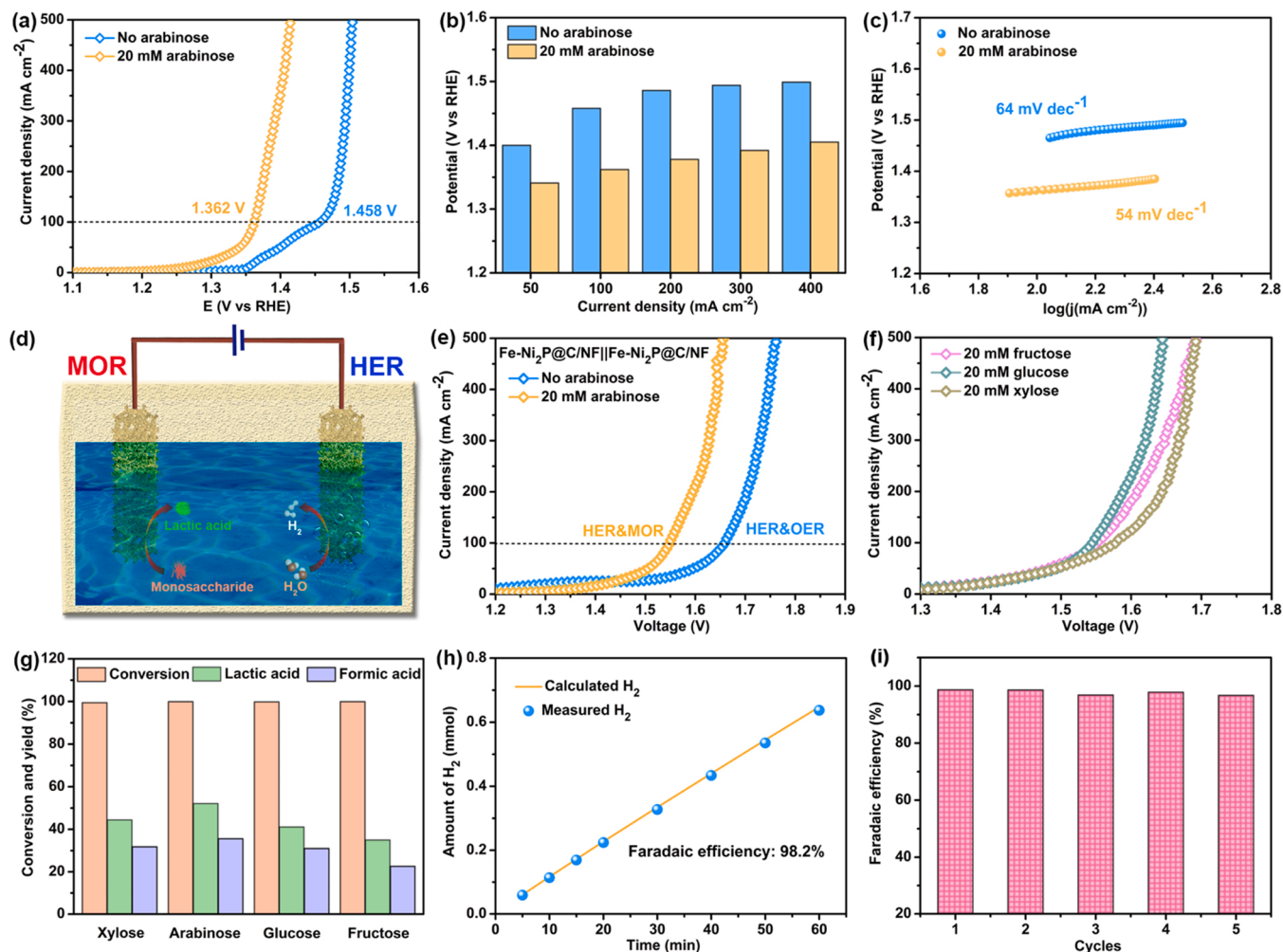


Fig. 5. (a) Polarization curves of Fe-Ni₂P@C/NF with and without 20 mM arabinose in 1 M KOH. (b) The corresponding potentials comparison at different current densities and (c) Tafel slopes of Fe-Ni₂P@C/NF in 1 M KOH with and without 20 mM arabinose. (d) Schematic illustration of an electrolyzer for electrolytic hydrogen and lactic acid productions from monosaccharide. (e) The polarization curves of Fe-Ni₂P@C/NF || Fe-Ni₂P@C/NF in 1 M KOH with and without 20 mM arabinose and (f) other monosaccharide. (g) The conversion of monosaccharide and yield of the oxidation production from different monosaccharide. (h) Comparison between experimental measurement and theoretical calculation of H₂ evolution. (i) Faradaic efficiency of the Fe-Ni₂P@C/NF for H₂ production under five cycles.

reusability of Fe-Ni₂P@C/NF for MOR, consecutive runs for electrocatalytic oxidation of monosaccharide under electrolyzer was conducted (Fig. S22). Obviously, the electrocatalytic activity of Fe-Ni₂P@C/NF is well maintained, indicating its excellent durability and organic resistance during the MOR process. After continuous electrolysis, the final oxidation

products (lactic acid and formic acid) in the chronoamperometry test from the monosaccharide at the anode were monitored using high-performance liquid chromatography (HPLC) (Fig. S23 and S24), and the conversion rate of monosaccharides and the yield of oxidized products were calculated by standard curves (Fig. S25). As shown in Fig. 5g, Fe-Ni₂P@C/NF possesses an excellent catalytic activity with the monosaccharide (xylose, arabinose, glucose, and fructose) conversion of above 99% and the lactic acid yield of 52.1% from arabinose oxidation. In addition, formic acid, another industrial intermediate with high chemical-added value, is also obtained from the anodic oxidation products with a yield of 35.6%. Based on the experimental results and previous reports [32,52], the possible conversion path for xylose oxidation was proposed (Fig. S26). First, the isomerization of xylose was performed to form intermediate, which was then converted to the glyceraldehyde and oxalic acid by the Retro-aldol reaction. Subsequently, glyceraldehyde was further oxidized to lactic acid, and the C-C bond of oxalic acid was broken to form formic acid. In addition, the xylose can be also oxidized to xylonic acid, followed by the α -oxidation or β -oxidation to form the intermediate, which can be further converted to formic acid by a series of oxidation reaction. In addition, Fig. 5h shows that a high Faradaic efficiency of 98.2% for the H₂ production in the system coupling with HER and MOR can be achieved, and maintained even after five cycles (Fig. 5i). To further understand the

electrocatalytic oxidation of monosaccharide by Fe-Ni₂P@C/NF electrode, the surface chemical composition and valence state of the Fe-Ni₂P@C/NF after MOR were further investigated by XPS (Fig. S27). Compared to the initial Fe-Ni₂P@C/NF, the typical peaks of Ni-P at 853.7 and 870.8 eV are disappeared while the peak at 857.3 eV is attributed to high-valent nickel species, suggesting the deep oxidation of the catalyst surface. In addition, the new peak for Ni-O bond at 530.6 eV further confirms the formation of oxidized nickel species during MOR process [29]. The high-valent of nickel oxides or oxyhydroxides formed by in situ electrochemical oxidation of Fe-Ni₂P@C/NF surface could be the actual catalytic active site for MOR. Above results indicate that the anodic monosaccharide oxidation can replace OER, which can not only further reduce the cell voltage of water splitting, but also produce additional high value-added chemicals at the anode.

3.5. Density functional theory (DFT) calculations

To further elucidate the intrinsic mechanism of the enhanced HER activity of Fe-Ni₂P@C/NF, density functional theory (DFT) calculations were conducted to unveil the effect of Fe atom doping. It is generally known that the initial step for HER in alkaline media is the adsorption and dissociation of water molecule on the surface of catalyst, which is considered to be the kinetic limiting step of the HER process [53]. The optimized structure models for the adsorption and dissociation of water molecule on the surface of Fe-Ni₂P and Ni₂P were constructed, as shown in Fig. 6a and Fig. S28. First, the adsorption energy of water molecule (ΔG_{H_2O}) on the Fe-Ni₂P and Ni₂P surface was calculated (Fig. 6b). Indeed, Fe-Ni₂P exhibits a more negative ΔG_{H_2O} value (−1.34 eV) than that of Ni₂P (−0.76 eV), revealing the effective H₂O adsorption on the

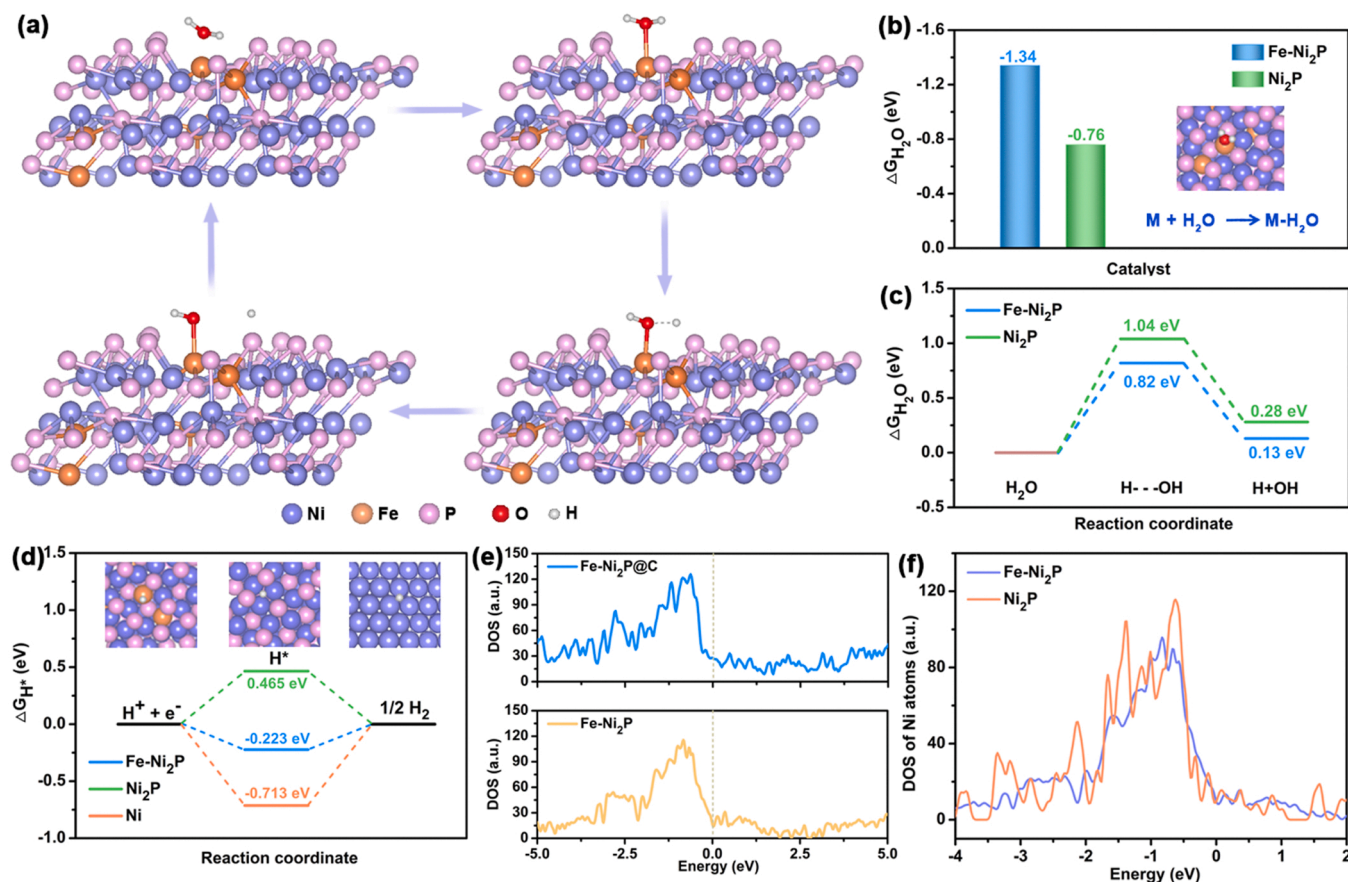


Fig. 6. (a) Schematic illustration of the water dissociation for the optimized structures models of Fe-Ni₂P in alkaline media. (b) DFT calculated the H₂O adsorption energy and (c) reaction free energy of the water dissociation on the Fe-Ni₂P and Ni₂P surfaces. (d) DFT calculated ΔG_{H^+} for Fe-Ni₂P, Ni₂P and Ni. (e) Calculated electronic density of states for Fe-Ni₂P@C and Fe-Ni₂P, and (f) Calculated DOS of Ni atoms in the Ni₂P structure prior to and after Fe doping.

Fe-Ni₂P surface, which is favorable to the subsequent dissociation step. Meanwhile, the energy barrier for the dissociation of H₂O on the surface of Fe-Ni₂P is 0.82 eV, which is significantly lower than that of Ni₂P (1.04 eV), indicating that the step of the H₂O dissociation on the Fe-Ni₂P surface to generate a proton can be obviously achieved after Fe doping (Fig. 6c). In addition, the free energy of H₂

adsorption (ΔG_{H^*}) is another key criterion for evaluating the performance of the electrocatalyst for HER, and the ΔG_{H^*} of an ideal electrocatalyst is thermally neutral ($\Delta G_{H^*} \approx 0$ eV). This indicates the balance between the adsorption of protons and the subsequent desorption of H₂ molecules from the active sites [54]. As shown in Fig. 6d, Ni₂P exhibits a calculated ΔG_{H^*} value of 0.465 eV, thus revealing the weak binding energy of protons on the Ni site, which is unfavorable to the formation of H_{ads} and further restricts the following reactions. Notably, after Fe doping, the ΔG_{H^*} value on the surface of Fe-Ni₂P decreases to -0.223 eV, which indicates that the Fe doping can optimize ΔG_{H^*} , thereby possessing a higher HER performance. This is consistent with the electrochemical test results discussed earlier. Meanwhile, the optimized adsorption structure models of H on the Fe, Ni and P sites of Fe-Ni₂P were constructed (Fig. S29), and the H₂ adsorption energies of the corresponding of different active sites were also calculated (Fig. S30). It can be seen that the ΔG_{H^*} values for the Ni (-0.324 eV) and Fe (-0.223 eV) sites of Fe-Ni₂P are more close to thermos-neutral compared with that for the Ni site of pure Ni₂P (0.465 eV). This further demonstrates the optimization of the adsorption energy of Ni₂P upon the introduction of Fe atoms. Moreover, the calculated ΔG_{H^*} values further reveal that the ΔG_{H^*} value of Fe-Ni₂P@C is effectively reduced to 0.086 eV compared to that of Fe-Ni₂P (-0.223 eV) (Fig. S31). This suggests that the synergistic effect of the carbon layer and Fe-Ni₂P can further optimize the ΔG_{H^*} during the HER process. The density of states (DOS) values of Fe-Ni₂P@C and Fe-Ni₂P were also calculated. As shown in Fig. 6e, the DOS of Fe-Ni₂P@C is higher than that of Fe-Ni₂P near the Fermi level, demonstrating that the carbon layer can enhance the conductivity of Fe-Ni₂P to boost the electron transfer rate during the HER process. In addition, the calculated partial DOS of Ni atom in Fe-Ni₂P and Ni₂P, shown in Fig. 6f, display a downshift of d-band center in Fe-Ni₂P after Fe doping. According to the d-band theory, a lower d-band center predicts the weakening of the binding strength between the proton and the active sites, which explains the weakened ΔG_{H^*} on the surface of Fe-Ni₂P [55,56]. The above DFT calculation results indicate that the introduction of Fe atoms can optimize the energy barrier of H₂O dissociation and ΔG_{H^*} . Moreover, the carbon layer can further enhance the conductivity of Fe-Ni₂P, thereby facilitating the HER process.

4. Conclusions

In summary, we developed a hierarchical structure of Fe-Ni₂P@C/NF bifunctional electrocatalyst with excellent electrochemical performance. The Fe-Ni₂P@C/NF catalyst exhibits high activity for HER with overpotentials of 75 and 313 mV to achieve the current density of 10 and 1000 mA cm⁻², respectively. The DFT calculations reveal that the remarkable catalytic performance of Fe-Ni₂P@C/NF can be attributed to the optimization of the electronic structure of Ni₂P by Fe atom doping and enhanced conductivity. In addition, a strategy of coupling HER with biomass-derived monosaccharide oxidation for simultaneous generation of H₂ and value-added lactic acid has also been developed by utilizing Fe-Ni₂P@C/NF as both cathodic and anodic catalysts. The cell voltage of the double-electrode can be further reduced to 1.55 V at 100 mA cm⁻² compared to overall water splitting. Significantly, this work also provides a strategy to design the transition-metal phosphides bifunctional electrocatalysts with advanced catalytic performance. Moreover, it provides an extension to the oxidation of other biomass to obtain high value-added lactic acid.

CRediT authorship contribution statement

Di Li: Conceptualization, Methodology, Investigation, Writing – original draft. **Zengyong Li:** Writing – review & editing, Formal analysis. **Ren Zou:** Investigation, Visualization. **Ge Shi:** Writing – review & editing. **Yiming Huang:** Formal analysis. **Wu Yang:** Formal analysis. **Wang Yang:** Formal analysis. **Chuanfu Liu:** Supervision, Visualization, Funding acquisition. **Xinwen Peng:** Supervision, Visualization, Writing – review & editing, Funding acquisition.

Declaration of Competing Interest

The authors declare that they have no known competing financial interests or personal relationships that could have appeared to influence the work reported in this paper.

Acknowledgments

This work was supported by Science and Technology Basic Resources Investigation Program of China (2019FY100900), State Key Laboratory of Pulp and Paper Engineering (2020ZR01), National Natural Science Foundation of China (22178128), National Program for Support of Top-notch Young Professionals, State Key Laboratory of Pulp and Paper Engineering Funds (2020C03), National Natural Science Foundation of China (31971614, 32071714 and 21736003), Guangzhou Science and Technology Funds (201904010078 and 202002030167).

Appendix A. Supporting information

Supplementary data associated with this article can be found in the online version at doi:10.1016/j.apcatb.2022.121170.

References

- [1] H. Wang, H.W. Lee, Y. Deng, Z. Lu, P.C. Hsu, Y. Liu, D. Lin, Y. Cui, Bifunctional non-noble metal oxide nanoparticle electrocatalysts through lithium-induced conversion for overall water splitting, *Nat. Commun.* 6 (2015) 7261.
- [2] H. Li, Q. Zhou, F. Liu, W. Zhang, Z. Tan, H. Zhou, Z. Huang, S. Jiao, Y. Kuang, Biomimetic design of ultrathin edge-riched FeOOH@Carbon nanotubes as high-efficiency electrocatalysts for water splitting, *Appl. Catal. B Environ.* 255 (2019), 117755.
- [3] Y. Pan, K. Sun, S. Liu, X. Cao, K. Wu, W.C. Cheong, Z. Chen, Y. Wang, Y. Li, Y. Liu, D. Wang, Q. Peng, C. Chen, Y. Li, Core-shell ZIF-8@ZIF-67-derived CoP nanoparticle-embedded N-doped carbon nanotube hollow polyhedron for efficient overall water splitting, *J. Am. Chem. Soc.* 140 (2018) 2610–2618.
- [4] Y. Xu, M. Kraft, R. Xu, Metal-free carbonaceous electrocatalysts and photocatalysts for water splitting, *Chem. Soc. Rev.* 45 (2016) 3039–3052.
- [5] J. Wang, F. Ciucci, In-situ synthesis of bimetallic phosphide with carbon tubes as an active electrocatalyst for oxygen evolution reaction, *Appl. Catal. B Environ.* 254 (2019) 292–299.
- [6] L. Ji, J. Wang, X. Teng, T.J. Meyer, Z. Chen, CoP nanoframes as bifunctional electrocatalysts for efficient overall water splitting, *ACS Catal.* 10 (2019) 412–419.
- [7] K. Wu, L. Zhang, Y. Yuan, L. Zhong, Z. Chen, X. Chi, H. Lu, Z. Chen, R. Zou, T. Li, C. Jiang, Y. Chen, X. Peng, J. Lu, An iron-decorated carbon aerogel for rechargeable flow and flexible Zn-air batteries, *Adv. Mater.* 32 (2020), e2002292.
- [8] Y. Huang, L. Hu, R. Liu, Y. Hu, T. Xiong, W. Qiu, M.S. Balogun, A. Pan, Y. Tong, Nitrogen treatment generates tunable nanohybridization of Ni₃P₄ nanosheets with nickel hydr(oxy)oxides for efficient hydrogen production in alkaline, seawater and acidic media, *Appl. Catal. B Environ.* 251 (2019) 181–194.
- [9] Y. Zhu, G. Chen, X. Xu, G. Yang, M. Liu, Z. Shao, Enhancing electrocatalytic activity for hydrogen evolution by strongly coupled molybdenum nitride@nitrogen-doped carbon porous nano-octahedrons, *ACS Catal.* 7 (2017) 3540–3547.
- [10] Y. Chen, J. Yu, J. Jia, F. Liu, Y. Zhang, G. Xiong, R. Zhang, R. Yang, D. Sun, H. Liu, W. Zhou, Metallic Ni₃Mo₃N porous microrods with abundant catalytic sites as efficient electrocatalyst for large current density and superstability of hydrogen evolution reaction and water splitting, *Appl. Catal. B Environ.* 272 (2020), 118956.
- [11] S. Wang, J. Wang, M. Zhu, X. Bao, B. Xiao, D. Su, H. Li, Y. Wang, Molybdenum-carbide-modified nitrogen-doped carbon vesicle encapsulating nickel nanoparticles: a highly efficient, low-cost catalyst for hydrogen evolution reaction, *J. Am. Chem. Soc.* 137 (2015) 15753–15759.
- [12] J. Zhou, S. Guo, Carbon-based anode materials for potassium-ion batteries: from material, mechanism to performance, *SmartMat* 2 (2021) 176–201.
- [13] Q.-s. Zhou, X.-w. Peng, L.-x. Zhong, R.-c. Sun, CoSe₂ nanobelt coupled with CoMoO₄ nanosheet as efficient electrocatalysts for hydrogen and oxygen evolution reaction, *Environ. Sci. Ecotechnol.* 1 (2020), 100004.

- [14] V. Kuraganti, A. Jain, R. Bar-Ziv, A. Ramasubramaniam, M. Bar-Sadan, Manganese doping of MoSe₂ promotes active defect sites for hydrogen evolution, *ACS Appl. Mater. Interfaces* 11 (2019) 25155–25162.
- [15] B. Guo, K. Yu, H. Li, R. Qi, Y. Zhang, H. Song, Z. Tang, Z. Zhu, M. Chen, Coral-shaped MoS₂ decorated with graphene quantum dots performing as a highly active electrocatalyst for hydrogen evolution reaction, *ACS Appl. Mater. Interfaces* 9 (2017) 3653–3660.
- [16] F. Shen, Y. Wang, G. Qian, W. Chen, W. Jiang, L. Luo, S. Yin, Bimetallic iron-iridium alloy nanoparticles supported on nickel foam as highly efficient and stable catalyst for overall water splitting at large current density, *Appl. Catal. B Environ.* 278 (2020), 119327.
- [17] B. You, X. Liu, N. Jiang, Y. Sun, A general strategy for decoupled hydrogen production from water splitting by integrating oxidative biomass valorization, *J. Am. Chem. Soc.* 138 (2016) 13639–13646.
- [18] H.G. Cha, K.S. Choi, Combined biomass valorization and hydrogen production in a photoelectrochemical cell, *Nat. Chem.* 7 (2015) 328–333.
- [19] Y. Liu, J. Zhang, Y. Li, Q. Qian, Z. Li, Y. Zhu, G. Zhang, Manipulating dehydrogenation kinetics through dual-doping Co₃N electrode enables highly efficient hydrazine oxidation assisting self-powered H₂ production, *Nat. Commun.* 11 (2020) 1853.
- [20] Q. Qian, J. Zhang, J. Li, Y. Li, X. Jin, Y. Zhu, Y. Liu, Z. Li, A. El-Harairy, C. Xiao, G. Zhang, Y. Xie, Artificial heterointerfaces achieve delicate reaction kinetics towards hydrogen evolution and hydrazine oxidation catalysis, *Angew. Chem. Int. Ed.* 60 (2021) 5984–5993.
- [21] B. Xia, J. Zhang, H. Wang, Y. Tian, Y. Yan, Q. Xue, T. He, H. Liu, C. Wang, Y. Chen, Substituted anodic hydrazine oxidation assisting energyefficient hydrogen production based on bifunctional cobalt perselenide nanosheet electrode, *Angew. Chem. Int. Ed.* 57 (2018) 7649–7653.
- [22] K. Xiang, D. Wu, X. Deng, M. Li, S. Chen, P. Hao, X. Guo, J.L. Luo, X.Z. Fu, Boosting H₂ generation coupled with selective oxidation of methanol into value-added chemical over cobalt hydroxide/hydroxysulfide nanosheets electrocatalysts, *Adv. Funct. Mater.* 30 (2020), 1909610.
- [23] B. You, X. Liu, X. Liu, Y. Sun, Efficient H₂ evolution coupled with oxidative refining of alcohols via a hierarchically porous nickel bifunctional electrocatalyst, *ACS Catal.* 7 (2017) 4564–4570.
- [24] S. Chen, J. Duan, A. Vasileff, S.Z. Qiao, Size fractionation of two-dimensional sub-nanometer thin manganese dioxide crystals towards superior urea electrocatalytic conversion, *Angew. Chem. Int. Ed.* 55 (2016) 3804–3808.
- [25] D. Liu, T. Liu, L. Zhang, F. Qu, G. Du, A.M. Asiri, X. Sun, High-performance urea electrolysis towards less energy-intensive electrochemical hydrogen production using a bifunctional catalyst electrode, *J. Mater. Chem. A* 5 (2017) 3208–3213.
- [26] Z.-Y. Yu, C.-C. Lang, M.-R. Gao, Y. Chen, Q.-Q. Fu, Y. Duan, S.-H. Yu, Ni–Mo–O nanorod-derived composite catalysts for efficient alkaline water-to-hydrogen conversion via urea electrolysis, *Energy Environ. Sci.* 11 (2018) 1890–1897.
- [27] Y. Huang, X. Chong, C. Liu, Y. Liang, B. Zhang, Boosting hydrogen production via anodic oxidation of primary amines over a NiSe nanorod electrode, *Angew. Chem. Int. Ed.* 57 (2018) 13163–13166.
- [28] G. Yang, Y. Jiao, H. Yan, Y. Xie, A. Wu, X. Dong, D. Guo, C. Tian, H. Fu, Interfacial engineering of MoO₂-FeP heterojunction for highly efficient hydrogen evolution coupled with biomass electrooxidation, *Adv. Mater.* 32 (2020), e2000455.
- [29] L. Gao, Z. Liu, J. Ma, L. Zhong, Z. Song, J. Xu, S. Gan, D. Han, L. Niu, NiSe@NiO_x core-shell nanowires as a non-precious electrocatalyst for upgrading 5-hydroxymethylfurfural into 2,5-furandicarboxylic acid, *Appl. Catal. B Environ.* 261 (2020), 118235.
- [30] W. Deng, H. Zhang, L. Xue, Q. Zhang, Y. Wang, Selective activation of the C–O bonds in lignocellulosic biomass for the efficient production of chemicals, *Chin. J. Catal.* 36 (2015) 1440–1460.
- [31] W. Deng, Q. Zhang, Y. Wang, Catalytic transformations of cellulose and cellulose-derived carbohydrates into organic acids, *Catal. Today* 234 (2014) 31–41.
- [32] S. Kiatphuegpor, A. Junkaew, C. Luadthong, S. Thongratkaew, C. Yimsukanan, S. Songtawe, T. Butburee, P. Khemthong, S. Namuangruk, M. Kunaseth, K. Faungnawakij, Roles of acidic sites in alumina catalysts for efficient D-xylose conversion to lactic acid, *Green Chem.* 22 (2020) 8572–8583.
- [33] M. Dusselier, P. Van Wouwe, A. Dewaele, E. Makshina, B.F. Sels, Lactic acid as a platform chemical in the biobased economy: the role of chemocatalysis, *Energy Environ. Sci.* 6 (2013) 1415–1442.
- [34] A. Corma, S. Iborra, A. Vely, Chemical routes for the transformation of biomass into chemicals, *Chem. Rev.* 107 (2007) 2411–2502.
- [35] A. Onda, T. Ochi, K. Kajiyoshi, K. Yanagisawa, A new chemical process for catalytic conversion of D-glucose into lactic acid and gluconic acid, *Appl. Catal. A Gen.* 343 (2008) 49–54.
- [36] L. Yang, J. Su, S. Carl, J.G. Lynam, X. Yang, H. Lin, Catalytic conversion of hemicellulosic biomass to lactic acid in pH neutral aqueous phase media, *Appl. Catal. B Environ.* 162 (2015) 149–157.
- [37] X. Yang, L. Yang, W. Fan, H. Lin, Effect of redox properties of LaCoO₃ perovskite catalyst on production of lactic acid from cellulosic biomass, *Catal. Today* 269 (2016) 56–64.
- [38] B. You, N. Jiang, X. Liu, Y. Sun, Simultaneous H₂ generation and biomass upgrading in water by an efficient noble-metal-free bifunctional electrocatalyst, *Angew. Chem. Int. Ed. Engl.* 55 (2016) 9913–9917.
- [39] N. Jiang, B. You, R. Boonstra, I.M. Terrero Rodriguez, Y. Sun, Integrating electrocatalytic 5-hydroxymethylfurfural oxidation and hydrogen production via Co–P-derived electrocatalysts, *ACS Energy Lett.* 1 (2016) 386–390.
- [40] X. Hu, S. Zhang, J. Sun, L. Yu, X. Qian, R. Hu, Y. Wang, H. Zhao, J. Zhu, 2D Fe-containing cobalt phosphide/cobalt oxide lateral heterostructure with enhanced activity for oxygen evolution reaction, *Nano Energy* 56 (2019) 109–117.
- [41] Y. Yang, X. Liang, F. Li, S. Li, X. Li, S.P. Ng, C.L. Wu, R. Li, Encapsulating Co₂P@C core-shell nanoparticles in a porous carbon sandwich as dual-doped electrocatalyst for hydrogen evolution, *ChemSusChem* 11 (2018) 376–388.
- [42] Y. Shi, Y. Xu, S. Zhuo, J. Zhang, B. Zhang, Ni₂P nanosheets/Ni foam composite electrode for long-lived and pH-tolerable electrochemical hydrogen generation, *ACS Appl. Mater. Interfaces* 7 (2015) 2376–2384.
- [43] B. Ma, Z. Yang, Y. Chen, Z. Yuan, Nickel cobalt phosphide with three-dimensional nanostructure as a highly efficient electrocatalyst for hydrogen evolution reaction in both acidic and alkaline electrolytes, *Nano Res.* 12 (2018) 375–380.
- [44] C. Zhu, Z. Yin, W. Lai, Y. Sun, L. Liu, X. Zhang, Y. Chen, S.-L. Chou, Fe–Ni–Mo nitride porous nanotubes for full water splitting and Zn–Air batteries, *Adv. Energy Mater.* 8 (2018), 1802327.
- [45] J. Lu, S. Yin, P.K. Shen, Carbon-encapsulated electrocatalysts for the hydrogen evolution reaction, *Electrochem. Energy Rev.* 2 (2019) 105–127.
- [46] G. Qian, J. Chen, T. Yu, L. Luo, S. Yin, N-doped graphene-decorated NiCo alloy coupled with mesoporous NiCoMoO nano-sheet heterojunction for enhanced water electrolysis activity at high current density, *Nano Micro Lett.* 13 (2021) 77.
- [47] S. Jing, J. Lu, G. Yu, S. Yin, L. Luo, Z. Zhang, Y. Ma, W. Chen, P.K. Shen, Carbon-encapsulated WOX hybrids as efficient catalysts for hydrogen evolution, *Adv. Mater.* 30 (2018), e1705979.
- [48] X. Luo, P. Ji, P. Wang, R. Cheng, D. Chen, C. Lin, J. Zhang, J. He, Z. Shi, N. Li, S. Xiao, S. Mu, Interface engineering of hierarchical branched Mo-doped Ni₂S₂/Ni₃P₂ hollow heterostructure nanorods for efficient overall water splitting, *Adv. Energy Mater.* 10 (2020), 1903891.
- [49] H. Liang, A.N. Gandi, C. Xia, M.N. Hedhili, D.H. Anjum, U. Schwingenschlögl, H. N. Alshareef, Amorphous NiFe–OH/NiFeP electrocatalyst fabricated at low temperature for water oxidation applications, *ACS Energy Lett.* 2 (2017) 1035–1042.
- [50] D. Das, K.K. Nanda, One-step, integrated fabrication of Co₂P nanoparticles encapsulated N, P dual-doped CNTs for highly advanced total water splitting, *Nano Energy* 30 (2016) 303–311.
- [51] L.-A. Stern, L. Feng, F. Song, X. Hu, Ni₂P as a Janus catalyst for water splitting: the oxygen evolution activity of Ni₂P nanoparticles, *Energy Environ. Sci.* 8 (2015) 2347–2351.
- [52] Y. Zhang, H. Luo, L. Kong, X. Zhao, G. Miao, L. Zhu, S. Li, Y. Sun, Highly efficient production of lactic acid from xylose using Sn-beta catalysts, *Green Chem.* 22 (2020) 7333–7336.
- [53] K. Xu, H. Cheng, H. Lv, J. Wang, L. Liu, S. Liu, X. Wu, W. Chu, C. Wu, Y. Xie, Controllable surface reorganization engineering on cobalt phosphide nanowire arrays for efficient alkaline hydrogen evolution reaction, *Adv. Mater.* 30 (2018), 1703322.
- [54] C. Guan, W. Xiao, H. Wu, X. Liu, W. Zang, H. Zhang, J. Ding, Y.P. Feng, S. J. Pennycook, J. Wang, Hollow Mo-doped CoP nanoarrays for efficient overall water splitting, *Nano Energy* 48 (2018) 73–80.
- [55] D. Zhao, K. Sun, W.C. Cheong, L. Zheng, C. Zhang, S. Liu, X. Cao, K. Wu, Y. Pan, Z. Zhuang, B. Hu, D. Wang, Q. Peng, C. Chen, Y. Li, Synergistically interactive pyridinic-N-MoP sites: identified active centers for enhanced hydrogen evolution in alkaline solution, *Angew. Chem. Int. Ed. Engl.* 59 (2020) 8982–8990.
- [56] Q. Zhou, Z. Shen, C. Zhu, J. Li, Z. Ding, P. Wang, F. Pan, Z. Zhang, H. Ma, S. Wang, H. Zhang, Nitrogen-doped CoP electrocatalysts for coupled hydrogen evolution and sulfur generation with low energy consumption, *Adv. Mater.* 30 (2018), 1800140.